Supplementary materials: emergent dynamics of active elastic microbeams

The supplementary material is divided into 9 sections. The first section concerns the description of additional files. Sec. S2-S5 include details on experimental procedures. The remaining sections are on the theories of the free beams and clamped beams. Unless otherwise stated, SI units are used throughout the supplemental.

S1. DESCRIPTION OF ADDITIONAL SUPPLEMENTARY FILES

File Name: Supplementary Movie 1

Description: **Assembly of active beams.** Self-propelled active colloids are assembled into beams of determined length N thanks to a pattern of optical traps, set by a spatial light modulator. Active beams of increasing lengths are obtained by extending the template of traps on both ends while continuously trapping the backbone of the structure. Optical traps template the assembly. After release, the active beam (N=15) remains stable owing to the (non-equilibrium) interactions of the active particles composing the materials and exhibit autonomous dynamics. The movie is sped up 10 times compared to real-time. Scale bar is $5\mu m$.

File Name: Supplementary Movie 2

Description: **Dynamics of active beams.** Active beams are solids made of active particles. They exhibit rich dynamics as visible on this movie. A free beam of short length (N=3) exhibits a persistent rotation, while a long beam (N=11) displays a stochastic rotation. The left and middle movies correspond respectively to the time evolution of the angle θ displayed in figure 3(A) and 3(B). When active beams (N=11) are clamped through optical traps at one end, the opposite end, free to move, exhibits oscillatory motion with a slow period above ten seconds. The right movie corresponds to the time evolution of the angle θ displayed in figure 2(B). Real-time movies. Scale bar is $5\mu m$.

S2. EXPERIMENTAL OPTICAL SETUP

A low-density solution of microswimmers is prepared in diluted hydrogen peroxide solution (6%) with deionized water. The sample is contained in a rectangular glass capillary and particles sediment at the bottom surface. Experiments are realized with a custom-made microscope. The activity of the microswimmers is controlled with a blue LED (425-500 nm). Assembly of the active particles into an active beam is realized with a pattern of optical traps with a red laser (639 nm) and a Spatial Light Modulator (Holoeye LETO). Imaging is recorded in transmission with a white lamp and a CCD camera at 30 fps.

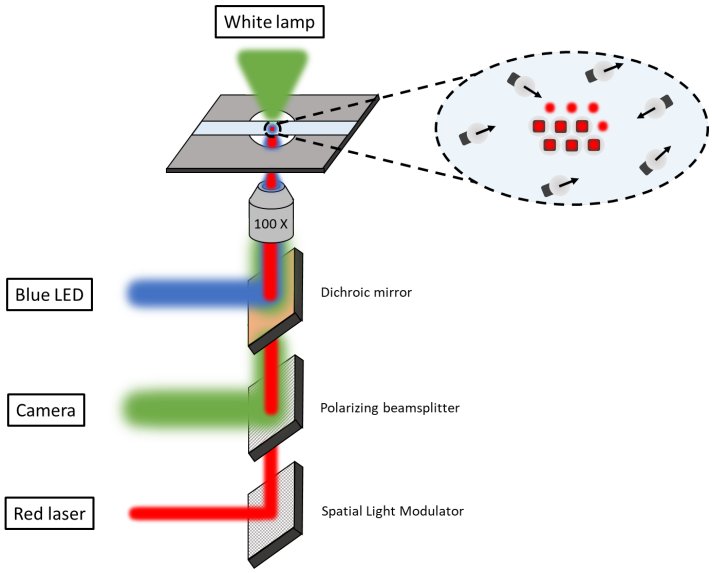

FIG. S1. Principle of the optical set-up with the main components.

The minimal size of an active beam (N = 3) is fully designed with a set of 10 optical traps. Thanks to the high diffusivity of the microswimmers, the pattern can be fully filled in tens of seconds. To grow larger active beams, only the central line of particles is fully trapped and optical traps are added on each side sequentially. This design allows us to reduce the optical power needed by reducing drastically the number of optical traps for long active beams (For N = 17 active beams, only 22 optical traps are required for a structure made of 52 microswimmers). When the desired length of the active beam is obtained, the optical traps are turned off to release it. The structure remains stable thanks to the activity of the particles and presents a dynamic depending on the length of the active beam and boundary conditions.

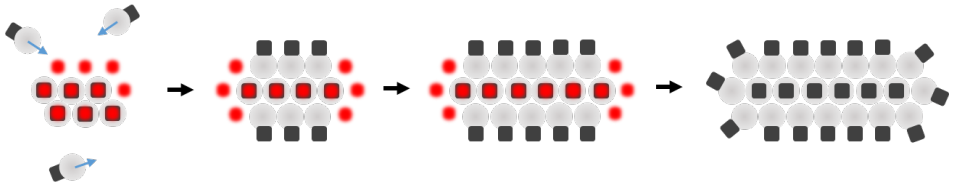

FIG. S2. Extension of the optical pattern to assemble long active beams.

S3. PERSISTENCE LENGTH MEASUREMENTS ON LONG ACTIVE BEAMS

Considering the small bending observed in the shape fluctuations of the active beams, the measurements of persistence length are only performed on the longer ones. The secant method is more ap-

propriate for materials with a small contour length (30 μm) compared to the persistence length (> 1 mm). The persistence length measurements of the active beams are realized over the range N = 11 – 17 corresponding to a contour length of 21 to 32 μm. Multiple independent measurements are realized for each size with a recording of the shape fluctuations over at least 3000 frames at 30 fps. For each frame, the positions of the microswimmers in the central line of the active beam are tracked. The different lengths of secant ℓ are considered and the distance δ from the central line of the active beam to the middle of each secant is measured. Over the full length of the recording, the mean square distance δ as a function of the length of the secant ℓ is fitted with $< \delta^2 > = \ell^3/(48\ L_p)$ to extract L_p [Fig.S3].

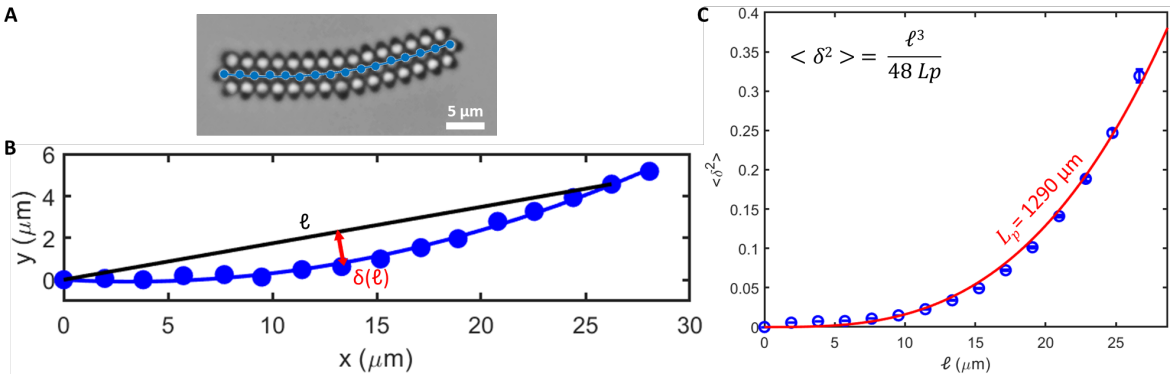

FIG. S3. (A) Brightfield image of an active beam (N = 15) with a clear bending of the structure. (B) Corresponding microswimmer positions of the central line. The black line corresponds to a secant ℓ = 14 microswimmers. The red line is the distance δ to the middle of the secant. (C) Mean square distance δ as a function of ℓ for this active polymer over 3000 frames. The red line corresponds to the fit of the experimental data, giving a persistence length L_p of 1290 μm.

S4. MICRO TENSILE TEST OF ACTIVE BEAMS

Both ends of the active polymer are clamped with 7 optical traps and the distance is modified by steps of 140 nm with the spatial light modulator. Positions of the traps are first tracked with the center of rotors on both sides for each step over 500 frames. The stiffness of the optical traps is measured with the equipartition theorem over 4000 frames, showing a good linearity with the laser power. Remarkably, for low activity of the microswimmers (by reducing the blue light intensity), the stiffness of the traps is decreased by 30 %. This effect is also verified with an independent stiffness measurement by dragging at 15 μm/s a single optically trapped microswimmer at high and low activity. The micro tensile tests are performed for 8 different active beams (N = 15) with a trap stiffness of 0.9 pN/μm. For the stress calculation, the cross-section is assumed to be a rectangle of 4.3 μm by 1.7 μm. It allows to stretch the active beam by 600 nm before it slides out of the optical traps or breaks. For the strain estimate, the original length of the active beam is measured when the optical forces are null. The micro tensile test is also realized for active beams at low activity of the active colloids ($\sim$ 75% light intensity). The beams also show then a linear elastic region with a reduced Young modulus of 22 Pa (down from 40Pa at maximal activity. This shows the tunability of the mechanical properties of this active material.

S5. POLARIZATION OF MICROSWIMMERS

In the active beams, active colloids can be classified into three categories [Fig. S6B]: on the side (yellow), the two at the extreme tip (blue), and the ones on the side of the tip (orange). Polarization of all the microswimmers can be tracked during an experiment of clamping beams. From the distribution of polarization, we can see that the microswimmers on the side of the active beams (yellow) have

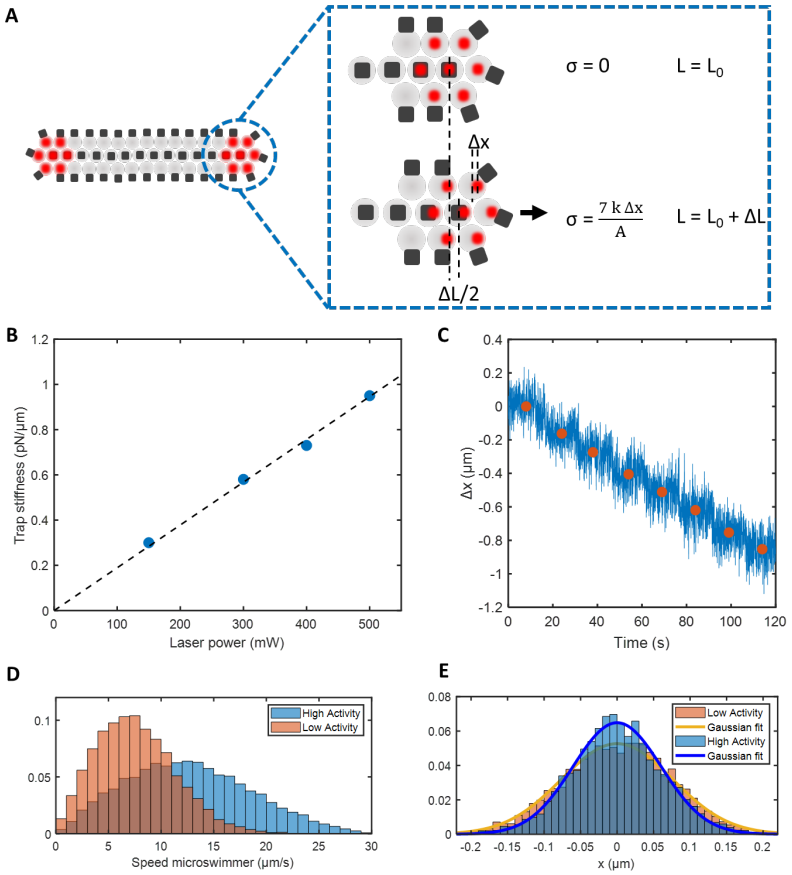

FIG. S4. (A) Principle of the microtensile test on active beams. Each end of the active beams is clamped with 7 optical traps. The force is calculated with the distance Δx between the position of the optical trap and the center of the microswimmer. The strain is obtained from comparing the extension of the beam with the extension when the optical forces are null. Those measures allow to obtain stress-strain curves as visible on the main text and perform tensile tests on the active beams. (B) Trapping stiffness of a microswimmer as a function of laser power. (C) Tracking positions of the optical trap during the extension of the pattern. The blue line corresponds to the tracked center position of the microswimmer and the orange dot is the mean position for each step of extension. Note that the extension is sub micrometric. (D) Effect of the light intensity on the activity of the active colloids, quantified by measuring the histogram of the velocity of the active colloids at two intensity levels of blue illumination (where low intensity is 75% of the maximal intensity of light). (E) Effect of the activity on the stiffness of the optical trap. For lower activity, a small broadening in the position of the microswimmer in the optical trap is observed.

a narrow distribution centered around 90 degrees. Their contribution to the bending of the active beam cancels out and is negligible. As shown for the free beams [see Main text], the dynamic can be understood quantitatively by considering only the orientation of the microswimmers at the extreme tip (blue). The orientation of the microswimmer on the side of the tip (orange) are highly correlated with the end one (blue) [Fig.S6C]. As visible with the cross correlation [Fig.S6D], the behavior of the beam is well captured by considering only the end colloid (blue) rather than the orange ones. In effect, we only consider the polarisation of the end (blue) colloid in our measurements and model.

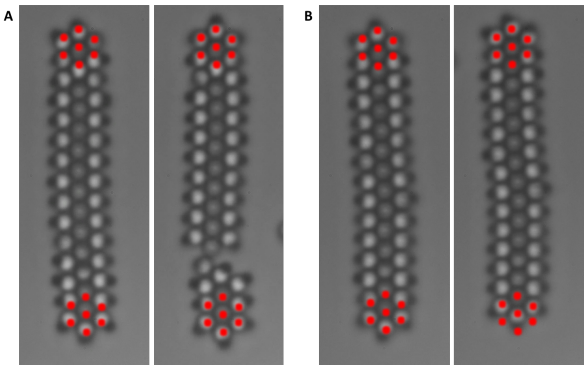

FIG. S5. Limit of extension for the micro tensile test on the active beam either with breaking (A) or sliding (B). On top of the brightfield images, the red dots indicate the positions of the optical traps.

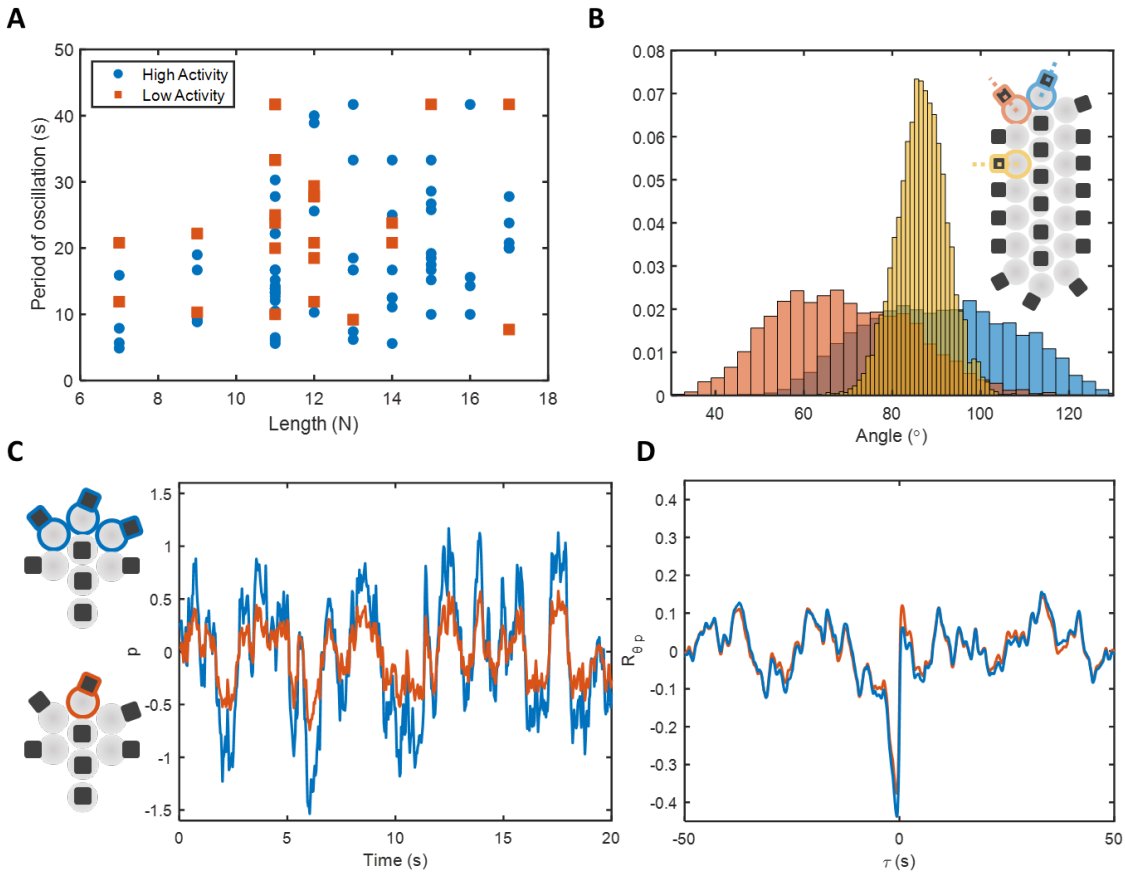

FIG. S6. (A) Period of oscillation of the clamped beams for high and low levels of activity. (B) Angular distribution of microswimmer on the side (yellow), on the side of the tip (orange), and at the extreme tip (blue) of a clamped beam (N=11). (C) Polarization p of the active beam clamped (N=11) considering the orientations of the three microswimmers at the tip (blue) or only one (orange). (D) Cross-correlation of the polarization p and the bending angle θ of the active beam clamped (N=11) considering the orientations of three microswimmers at the tip (blue) or only one (orange).

S6. THEORY OF FREE ACTIVE BEAMS

This section further develops the theory and modeling described in the main text. While there are overlaps with the main text, we provide a self-contained section on the theory of free beams to include more theoretical details and mathematical nuances.

Having established the Active Ornstein-Uhlenbeck process (AOUP) as an effective model for individual swimmers and the interactions of an individual swimmer and the background fluid, we proceed to formalize a simple model for free beams.

For simplicity, we model a free beam as driven only by swimmers at the tip, as illustrated in Fig. 3E of the main text. Force balance requires

$$\chi_s R^3 \partial_t \theta = \mu R(p_1 + p_2) + R\sigma_\theta \Lambda_\theta \tag{S1}$$

$$\partial_t p_1 = f(R\partial_t\theta, p_1) - \gamma p_1 + \sqrt{\gamma}\Lambda_1 \tag{S2}$$

$$\partial_t p_2 = f(R\partial_t\theta, p_2) - \gamma p_2 + \sqrt{\gamma}\Lambda_2 \tag{S3}$$

where $\chi_s R^3$ represents the frictional moment of inertia, μ is the force exerted by one swimmer on the free beam, and $f(R\partial_t\theta, p_1)$ represents the interaction between p_1, the surrounding fluid, and the remaining swimmers. As before, $\Lambda_{\theta,1,2}$ are spatio-temporal white noises with unit variances. Here we take $p_{1,2}$ to be the projection of swimmer orientation perpendicular to the long axis of the beam. For simplicity, we neglect all contributions from the component parallel to the long axis as it simply follows a Gaussian distribution and does not have any additional interesting dynamics

As our system is in Stokes flow, we can compute χ_s directly using lubrication theory or exact solutions of a cylinder next to a wall [1]: for a cylindrical object at distance ξ near a no-slip boundary (Note that ξ is the distance between the bottom of the cylinder to the boundary. The distance from the center line of the cylinder to the boundary is $\xi + l_0$), we have $\chi_s = \frac{8\pi\eta}{3\sqrt{2\xi/l_0}}$ for $\xi \ll l_0$, where l_0 is roughly the radius of the cross-section of the cylinder. Since we have three swimmers in a row in the cross-section, we take an l_0 such that $2\pi l_0$ is the circumference: $l_0 \approx$ diameter of a swimmer. Now let N be the number of swimmers along the long axis ($N = 2R/l_0$), and observe that eq. (S1) implies that $N^2\partial_t\theta = s(p_1 + p_2)/2 +$ noise, where $s = \frac{8\mu}{\chi_s l_0^2}$. Since we can measure both the angular velocity $\partial_t\theta$ and (p_1, p_2) from experiments, this is an easily testable quantitative prediction, as well as a qualitative test for the fact that our polarity measurements are physically meaningful. As shown in Figure S7, measurements from all free beams of different lengths collapse onto the same straight line as predicted. The best-fit value for s is 55 ± 3; the error bar comes from statistical bootstrapping.

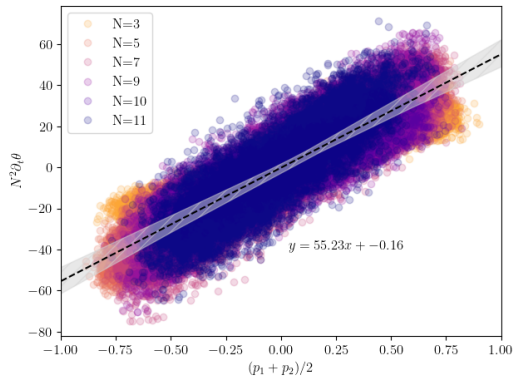

FIG. S7. Measurements from beams of 6 different lengths collapse onto the same straight line. Within experimental errors, the line goes through the origin as predicted by eq. S1. The shaded white region indicates the error bars obtained from bootstrapping statistics. Note that the errors are *not* the same residuals of linear regression but highlight variations in the *best-fit* parameters in statistical bootstrapping.

Next, to pin down the form of $f(\partial_t\theta, p_{1,2})$, we recall from eq.3 of the main text that the upstream re-orientation for particles with asymmetric shape is $\nu\dot{\gamma}\sin(\phi)$, where ν is a dimensionless parameter that represents the amount of asymmetry in the swimmer shape. $\dot{\gamma}$ is the local shear rate, which is approximately $R\partial_t\theta/\xi$, where ξ represents the length of the boundary layer. Recall also that ϕ denotes the angle between the swimming direction and the flow, which we approximate as $\sin(\phi) \approx O(1)$ as we are neglecting the dynamics of the component parallel to the beam. Additionally, the swimmer directions are constrained by neighbors due to the geometry of the active assembly, which we represent phenomenologically with a negative third-order term. Thus, overall we have

$$f(R\partial_t\theta, p) = \alpha R\partial_t\theta - \beta p^3 \tag{S4}$$

where we have absorbed ν, ξ into the definition of $\alpha = \nu/\xi$ for conciseness.

Let $p = (p_1 + p_2)/2$ and given that deviations of $p_{1,2}$ from p are small, as demonstrated in Fig. S6(C), we can add up the equations for p_1 and p_2 together to obtain approximately

$$\partial_t p = \left(\frac{\bar{\alpha}}{N} - \gamma\right) p - \beta p^3 + \sqrt{\gamma/2}\Lambda \tag{S5}$$

where $\bar{\alpha} = \alpha s l_0/2$ and the noise variance is $\gamma/2$ from the property of the mean of independent Gaussian noises. Observe that as we increase N, the linear term goes from positive to negative, marking a supercritical pitchfork bifurcation from two fixed points to one. This is indeed what we observe in experiments, as shown in Figure S8 and Fig. 3 of the main text – shorter beams tend to spin at some finite angular velocity with occasional reversals, whereas longer beams spin stochastically but more centered around zero.

Now that we have a qualitative understanding of the transition from persistent spinning to random active fluctuations, we proceed to seek quantitative agreements between theory and experiments. Since eq. (S5) is a single-variable stochastic differential equation, we solve for the steady state probability directly:

$$-\log P(p) = \frac{4}{\gamma}\left[\frac{1}{2}\left(\frac{\bar{\alpha}}{N} - \gamma\right)p^2 + \frac{\beta}{4}p^4\right] + \text{constant} \tag{S6}$$

Then we minimize $-\log P$ to find the best-fit parameters using data from free beams of 6 different lengths, as shown in Figure S8. This is known as the maximum likelihood method, a well-established stochastic inference method in statistics [2]. To estimate the errors in the parameters, we perform bootstrapping statistics to sample with replacement 100 times for each fitting scheme. Including the linear regression, the best-fit parameters are shown in Table S1. We now refer back to Sec. 3.4 of the main text for discussions of the results.

Parameter	s	$\frac{4}{\gamma}\bar{\alpha}$	$\frac{4}{\gamma}\beta$
MLE	55 ± 3	81 ± 16	56 ± 10
Direct estimates	17 ± 2	$699\nu \approx 70$	N/A

TABLE S1. Same as Table I of the main text, reproduced here for ease of reading. SI units are used for all parameters. For the direct estimates, we use the following formula $\bar{\alpha} = \alpha s l_0/2, s = \frac{8\mu}{\chi_s l_0^2}, \chi_s = \frac{8\pi\eta}{3\sqrt{2\xi/l_0}}$

S7. MINIMAL MODEL OF AN ELASTIC BEAM SUBJECT TO ACTIVE NOISE

In this section, we take a brief detour to investigate the scenario without the hydrodynamic coupling between the flow and the swimmer direction. In experiments, we observe a time scale of approximately 10s in the dynamics of the clamped beams. Thus we ask whether the dynamics could be produced by a minimal theory of an elastic beam subject to active noise with a persistence time of 10s.

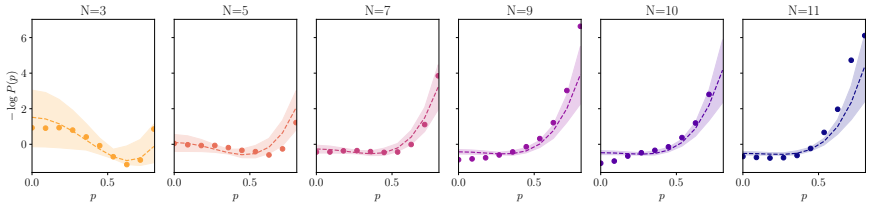

FIG. S8. log of the steady-state probability of free beams of 6 different lengths. The solid points are measurements from experiments and the dashed lines are predictions from Maximum Likelihood parameter fit. The parameters are constrained to be the same for all beams while N varies in eq. (S6)

Using the Euler-Bernoulli equation of beams, and the same assumption of the beam driven by swimmers at the tips, we arrive at the following minimal model,

$$\begin{aligned} \chi_b \partial_t \theta(x,t) &= -B\partial_x^4\theta + \frac{\mu}{L}\delta(x-L)p + L^{-1}\sqrt{2k_\mathrm{B}T^*\chi_b}\Lambda_\theta \\ \partial_t p &= -\gamma p + \sqrt{\gamma}\Lambda_p \\ \text{with boundary conditions: } \theta|_{x=0} &= 0,\ \partial_x\theta|_{x=0} = 0,\ \partial_x^2\theta|_{x=L} = 0,\ \partial_x^3\theta|_{x=L} = 0 \end{aligned} \tag{S7}$$

where $\Lambda_{\theta,p}$ are unit white noises. Here B is the bending modulus and $B = EI$, where E is Young's Modulus and I is the second moment of area about the bending axis: $I \approx 0.08\pi l_0^4$ if we approximate the cross-section as an ellipse of widths $(\sqrt{3}l_0, l_0)$ along its major and minor axes (since the center of mass of the side swimmers are $\sqrt{3}/2l_0$ away from the central axis). Additionally, χ_b represents the Stokes friction per unit length. From the exact solutions of the cylinder close to the wall [1], $\chi_b = \frac{4\pi\eta}{\sqrt{2\xi/l_0}}$ for $\xi \ll l_0 \ll L$, where η is viscosity and l_0 parameterizes the radius of the cross-section as before. From the persistence length L_p measurements, we know that fluctuations along the beam are much higher than thermal fluctuations, which we parameterize with the same effective temperature as experimentally inferred: $T^* = 4.7 \times 10^3 K$.

Rescaling space $x' = x/L$ and relabelling $x' \to x$ for convenience, we obtain

$$\partial_t\theta(x,t) = -\frac{B}{\chi_b L^4}\partial_x^4\theta + \frac{\mu}{\chi_b L^2}\delta(x-1)p + L^{-3/2}\sqrt{2k_\mathrm{B}T^*/\chi_b}\Lambda_\theta \tag{S8}$$

$$\partial_t p = -\gamma p + \sqrt{\gamma}\Lambda_p \tag{S9}$$

Since the first equation is linear, we are free to change the basis to any orthonormal set of functions. The most sensible choice here is the eigenfunctions of the bending operator ∂_x^4 obeying the same boundary conditions [3],

$$g_n(x) = \cosh k_n x - \cos k_n x + \frac{\cos k_n + \cosh k_n}{\sin k_n + \sinh k_n}(\sin k_n x - \sinh k_n x) \tag{S10}$$

where $k_0 \approx 0.6\pi, k_1 \approx 1.5\pi, k_2 \approx 2.5\pi$ and so on. We can now expand $\theta(x,t)$ in the basis of $\{g_n\}$ as $\theta(x,t) = \sum_n \theta_n(t)g_n(x,t)$, or conversely $\theta_n(t) = \int dx\ \theta(x,t)g_n(x)$ using orthogonality of the basis.

The corresponding eigenvalues are $\lambda_n = -\frac{B}{\chi L^4}k_n^4$. Notice that the first eigenvalue is already much larger in magnitude compared to the zeroth eigenvalue as $\lambda_1/\lambda_0 \approx 81$, which, combined with our experimental observation of the lack of higher order variations along the beam, justifies projecting the dynamics onto the zeroth mode only. Substituting in the same form of f as before and relabelling $\theta_0 \to \theta$ for brevity, we have

$$\begin{aligned} \partial_t\theta &= -\epsilon\theta + \bar{\mu}p + \bar{\Lambda}_\theta \\ \partial_t p &= -\gamma p + \bar{\Lambda}_p \end{aligned} \tag{S11}$$

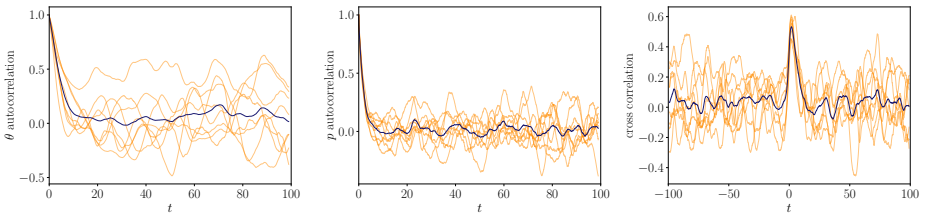

FIG. S9. Autocorrelations and crosscorrelations of a hypothetical minimal model that only includes elastic response and active driving by the swimmers at the tip. Note that the cross-correlations only show a peak at positive t but not negative t.

where $\epsilon = -\lambda_0 = \frac{B}{\chi_b L^4}(0.6\pi)^4$ and $\bar{\mu} = \frac{\mu g_0(1)}{\chi_b L^2}$. Observe that the equations, as written, are linear and therefore the deterministic dynamics are solely governed by the eigenvalues of the Jacobian matrix $\mathbf{J}$,

$$\mathbf{J} = \begin{pmatrix} -\epsilon & \bar{\mu} \\ 0 & -\gamma \end{pmatrix} \tag{S12}$$

We read off the eigenvalues as $(-\epsilon, -\gamma)$, since the matrix is upper-triangular. This implies that $(\theta, p) = (0, 0)$ is always a stable fixed point of the dynamics and therefore no oscillations are possible. Further, due to the lack of feedback from θ back to p, even if we force the persistence time to be comparable to the oscillation periods observed experimentally ($\sim 10s$ - despite the fact that single active particles display much smaller persistence time), the cross-correlation functions of this model (Fig. S9) only show a positive peak whereas that of the data show both a positive and negative peak (Fig. 4E of the main text and Fig. S13).

S8. THEORY OF CLAMPED BEAMS

Having explored an alternative scenario with no feedback and concluded that some form of feedback is required to produce dynamics seen in experiments, we now include hydrodynamics as the most minimal coupling, based on first physical principles, in the theory of clamped beams. This section supplements Sec. 3.5 of the main text.

Adding a hydrodynamic feedback to Eq. S7, we obtain

$$\begin{aligned} \chi_b \partial_t \theta(x,t) &= -B\partial_x^4 \theta + \frac{\mu}{L}\delta(x-L)p + L^{-1}\sqrt{2k_\mathrm{B}T^*\chi_b}\Lambda_\theta \\ \partial_t p &= f(L\partial_t\theta|_{x=L}, p) - \gamma p + \sqrt{\gamma}\Lambda_p \\ \text{with boundary conditions: } \theta|_{x=0} &= 0,\ \partial_x\theta|_{x=0} = 0,\ \partial_x^2\theta|_{x=L} = 0,\ \partial_x^3\theta|_{x=L} = 0 \end{aligned} \tag{S13}$$

where we've added the coupling term f to the second equation of eq. (S7). Rescaling space $x' = x/L$ and relabelling $x' \to x$ for convenience, we obtain

$$\partial_t \theta(x,t) = -\frac{B}{\chi_b L^4}\partial_x^4\theta + \frac{\mu}{\chi_b L^2}\delta(x-1)p + L^{-3/2}\sqrt{2k_\mathrm{B}T^*/\chi_b}\Lambda_\theta \tag{S14}$$

$$\partial_t p = f(L\partial_t\theta|_{x=1}, p) - \gamma p + \sqrt{\gamma}\Lambda_p \tag{S15}$$

Using the same orthonormal basis as before and only keeping the lowest mode, we have

$$\begin{aligned} \partial_t\theta &= -\epsilon\theta + \bar{\mu}p + \bar{\Lambda}_\theta \\ \partial_t p &= -(\gamma - c\bar{\mu})p - \beta p^3 - c\epsilon\theta + \bar{\Lambda}_p \end{aligned} \tag{S16}$$

where $\epsilon = -\lambda_0 = \frac{B}{\chi_b L^4}(0.6\pi)^4$ and $\bar{\mu} = \frac{\mu g_0(1)}{\chi_b L^2}$, and $c = \alpha L g_0(1)$. Importantly, since we substituted the first equation into the second, the two noises are no longer independent: $\left\langle \bar{\Lambda}_\theta(t)\bar{\Lambda}_p(t')\right\rangle = \delta(t-t')c\sigma_\theta^2$

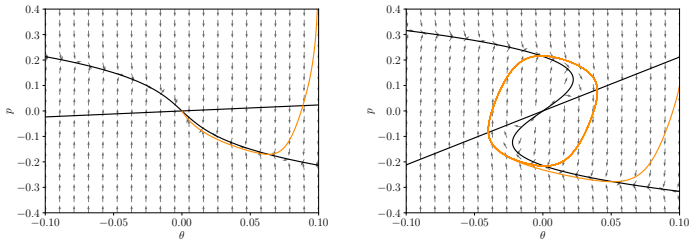

(a) One stable fixed point (b) Limit cycles

FIG. S10. Three types of dynamics of eq. (S16). The solid black lines are the nullclines, the arrows indicate local flow velocity and the orange lines are sample trajectories without stochasticity. All simulations are performed with $\epsilon = 0.17, \gamma = 0.75, c = 17, \beta = 17$. The remaining parameters are (a) $\bar{\mu} = 0.01$ (b) $\bar{\mu} = 0.09$.

, $\left\langle \bar{\Lambda}_p(t)\bar{\Lambda}_p(t')\right\rangle = \delta(t-t')(\gamma + c^2\sigma_\theta^2)$ and $\left\langle \bar{\Lambda}_\theta(t)\bar{\Lambda}_\theta(t')\right\rangle = \delta(t-t')\sigma_\theta^2$, where we have defined $\sigma_\theta = L^{-3/2}\sqrt{2k_\mathrm{B}T^*/\chi_b}$. In the literature, eq. S16 are known as the FitzHugh-Nagumo Model, commonly used to model neuron activities [4, 5]. The equations describe an excitable system that can undergo a Hopf bifurcation to admit limit-cycle solutions. To see this more clearly, let $\mathbf{J}$ be the Jacobian of the deterministic part of the coupled equations,

$$\mathbf{J} = \begin{pmatrix} -\epsilon & \bar{\mu} \\ -c\epsilon & -(\gamma - c\bar{\mu}) \end{pmatrix} \tag{S17}$$

Spot that the origin, $(\theta, p) = (0, 0)$, is a fixed point of the dynamics. Let $\lambda = \lambda_r + i\lambda_i$ be the eigenvalue of $\mathbf{J}$ with a larger real part. If $\lambda_r < 0$, the origin is a stable fixed point; conversely, if $\lambda_r > 0$, the system can undergo a Hopf bifurcation into stable limit cycles if $\lambda_i \neq 0$ (even if $\lambda_i = 0$, sometimes the system still settles into stable limit cycles due to structure of the nullclines. In this paper we will not distinguish between the two subcases of limit cycles). These two scenarios are illustrated in Figure S10 and a full phase diagram is shown in Fig. 4B of the main text.

A necessary (although not sufficient) condition for the origin to be unstable is that $(\gamma - c\bar{\mu}) < 0$. For a beam of length Nl_0, with the clamping by the optical trap, the effective length of the beam is $(N-1)l_0$ – from the center of the trap to the center of the swimmer at the tip (see Fig. 1B and Fig. 2A of the main text). Hence, we have $c\bar{\mu} = \frac{g_0^2}{6}\frac{\bar{\alpha}}{N-1} = \frac{80g_0^2}{24(N-1)}\gamma$ after substituting in the best-fit value for α from measurements of free beams. This means that for any $N < 14.5$, we have $(\gamma - c\bar{\mu}) < 0$, and the system can admit stable limit cycles at the deterministic level.

Following this preliminary analysis, we will now take a step further by using the remaining best-fit parameters of the free beams as well as direct measurements on the experimental setup. Recall that ML estimation of free beams measurements (Table S1) gives us three degrees of freedom, roughly corresponding to $\bar{\mu}, c/\gamma, \beta/\gamma$ here. This still leaves us with 3 parameters that we have to estimate from independent measurements: $\epsilon, \gamma, \sigma_\theta$. As will be elaborated further in Section S9, we estimate $\epsilon = 0.35, \gamma = 1$ (SI units) from mechanical and kinematic experiments, and $\sigma_\theta = 0.03$ (SI units) from thermal fluctuations. These are summarized in Table S2.

A. Qualitative comparison with experimental data

To test our model against experimental data, we measured (θ, p) for independent active beams of length $N = 11$. The (p, θ) distributions of experimental measurements are shown in Figure S11, showing mostly Gaussian-like distributions in both θ and p. The shapes of distributions in all three panels are well-matched by the simulations of the preliminary estimates in Table S2, as shown in Figure S12. It is perhaps puzzling that even though the preliminary estimates in Table S2 give rise to

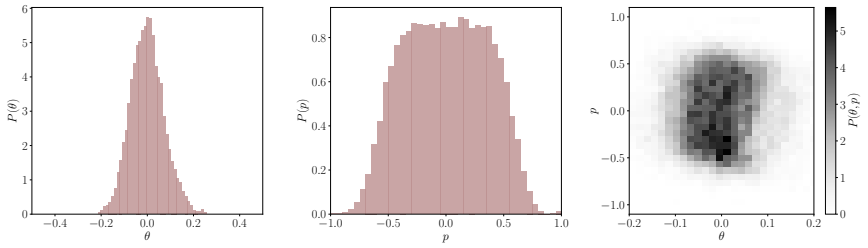

FIG. S11. (p, θ) distribution of experimental data from all 11 clamped beams. θ is sharply peaked whereas p follows a more broad peak that falls off quickly near $\pm$ 1.

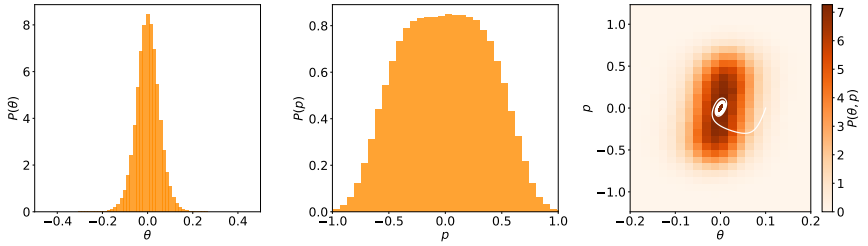

FIG. S12. (θ, p) distributions using preliminary estimates in Table S2. A deterministic limit-cycle trajectory is plotted in orange in the third panel.

deterministic limit cycles, we do not see distinguishable cycles in (p, θ) space. However, as we can see from the third panel of Figure S12, the deterministic limit cycles are obscured by the noise in both θ and p and the distribution completely covers the inside of the cycle. There are hints at the existence of the limit cycles: the peak of the p distribution is slightly flattened compared with the classic bell-shape of Gaussian distributions of the same width, a feature shared by both data and simulations.

Next, we will compare correlations between experiments and preliminary simulations. The correlations in data are shown in Figure S13. Both auto correlations are normalized with the value at $t = 0$ (the same as the average variance). The cross-correlation is defined as $\langle \theta(s)p(s+t) \rangle_s / \sqrt{\langle \theta(s)^2 \rangle_s \langle p(s)^2 \rangle_s}$

Even though individual trajectories show prominent, sometimes almost periodic, secondary peaks in θ auto-correlation for nonzero t, there is not an obvious time scale after averaging all the trajectories, hinting that the deterministic oscillations are obscured by noise. Another key feature of the data is that, in the cross-correlation, there is a sharp positive peak at approximately $t = 0.5s$ and a sharp negative peak at $t = -0.5s$ of similar magnitude. As demonstrated in Figure. S14, when we switch off cross-coupling in the J matrix by either setting $\bar{\mu}$ or c to zero, the shape of the peaks in cross-correlation is dramatically changed. Decreasing c drastically decreases the prominence of the 0_- peak

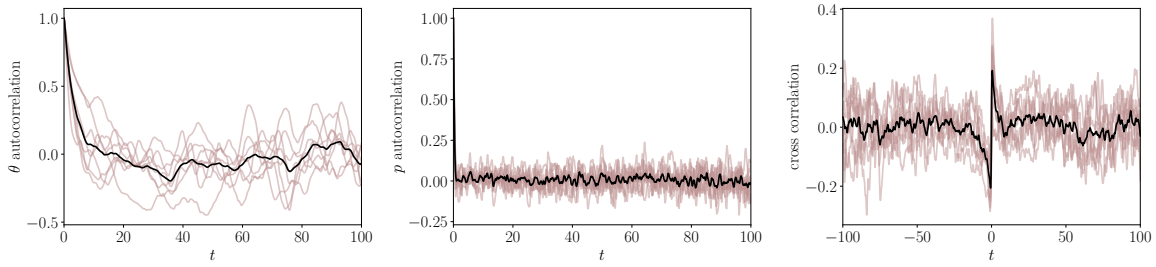

FIG. S13. Auto-correlations and cross-correlations of experimental measurements of θ and p for 11 beams of the same length. The orange lines correspond to individual beams and the blue line is the average.

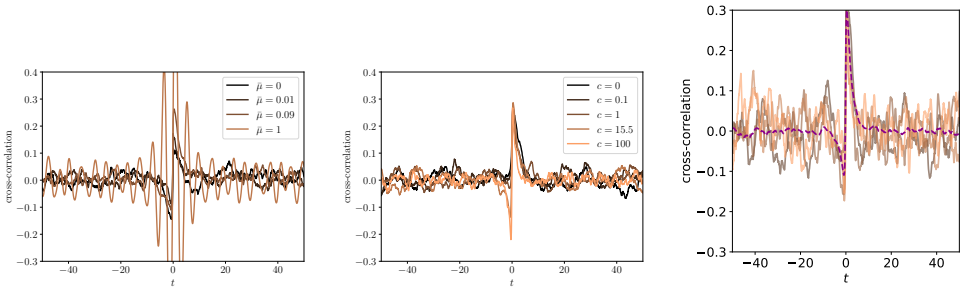

(a) $\bar{\mu}$ variations (b) c variations (c) Parameter estimates

FIG. S14. (a, b): Mean cross-correlations as we vary c, $\bar{\mu}$, corresponding to varying the magnitude of either cross term in the J matrix. (c) Setting both c and μ to the same values as the ML estimates of free beans (the mean cross-correlation plotted here is the average of 100 numerical simulations). The remaining parameters are the same as Table S2.

while having little effect on the 0_+ peak. Decreasing $\bar{\mu}$ decreases the size of both peaks but increasing $\bar{\mu}$ leads to clear oscillations that stand out against the noisy background. This confirms that both upstream reorientation (c) and the self-propulsion of active swimmers ($\bar{\mu}$) are critical in the observed behavior of clamped beams.

B. Parameter inference with measurement errors

Having established a qualitative understanding of our model and obtained a preliminary set of parameters that match well with data by eye, we were curious to see whether we are close to the best-fit parameters without any prior. Since Eq. (S16) is nonlinear, we cannot solve for the trajectory probabilities exactly, but as long as the time steps are small, we can still estimate the transition probability for each step accurately. More precisely, let $\mathbf{x} = (\theta, p)$ and $\{t_n\}$ be the measurement time points, we can compute $P(\mathbf{x}(t_{n+1})|\mathbf{x}(t_n))$ as long as $t_{n+1} - t_n$ is small. Firstly, we write the stochastic equation more concisely as

$$\partial_t \mathbf{x} = \mathbf{v}(\mathbf{x}) + \mathbf{\Lambda}, \quad \langle \mathbf{\Lambda}(t)\mathbf{\Lambda}^\intercal(t')\rangle = \mathbf{B} \tag{S18}$$

where $\mathbf{v}$ denotes the deterministic part of Eq. S16 and $\mathbf{B}$ is the noise kernel,

$$\mathbf{B} = \begin{pmatrix} \sigma_\theta^2 & c\sigma_\theta^2 \\ c\sigma_\theta^2 & c^2\sigma_\theta^2 + \sigma_p^2 \end{pmatrix} \tag{S19}$$

Now, using the definition of stochastic differential equations [6], we have

$$\begin{aligned} -\log \mathcal{P}\left[\mathbf{x}(t_{n+1})|\mathbf{x}(t_n)\right] &= \frac{1}{2}\log|2\pi\mathbf{\Sigma}| + \frac{1}{2}\mathbf{D}^\intercal\mathbf{\Sigma}^{-1}\mathbf{D} \\ \text{where } \mathbf{D} = \mathbf{x}(t_{n+1}) - \left[\mathbf{x}(t_n) + \mathbf{v}(\mathbf{x}(t_n))\Delta t\right],\ \mathbf{\Sigma} &= \mathbf{B}\Delta t \end{aligned} \tag{S20}$$

where $\Delta t = t_{n+1} - t_n$. The probability of an observed trajectory is then calculated as a product of conditional probabilities for each time step, or a sum after taking the log: $-\log\mathcal{P}[\{x(t_n)\}] = -\sum_n \log P\left[\mathbf{x}(t_{n+1})|\mathbf{x}(t_n)\right]$. Finally, we find the best-fit parameters by minimizing $-\log\mathcal{P}$ with respect to the parameters.

However, in our system, simply minimizing $-\log\mathcal{P}$ as defined above does not yield trajectories similar to experimental observations. This is because we also need to account for measurement error: we estimate a measurement error of 1% and 7% respectively in θ and p from pixelation in live imaging. For

linear stochastic differential equations, measurement errors can be accounted for exactly via Kalman filters. For nonlinear stochastic differential equations, no exact solutions exist but the Extended Kalman filter, which linearizes about an estimate of the current mean and covariance, is considered to be standard practice [7].

Firstly, we will unpack the problem of parameter inference with measurement errors. Let $\tilde{\mathbf{x}}_n$ be the measured value at time t_n and $\mathbf{x}_n$ be the true value at the same time point, by the definition of conditional probabilities, we have

$$P\left[\tilde{\mathbf{x}}_{n+1}|\tilde{\mathbf{x}}_n\right] = \int \mathrm{d}\mathbf{x}_{n+1}\mathrm{d}\mathbf{x}_n \; P\left(\tilde{\mathbf{x}}_{n+1}|\mathbf{x}_{n+1}\right) P(\mathbf{x}_{n+1}|\mathbf{x}_n) P(\mathbf{x}_n|\tilde{\mathbf{x}}_n) \tag{S21}$$

The first term is a simple Gaussian distribution around the true values and the second term has been computed previously in eq. S20. The last term is tricky because by Bayes' theorem,

$$P(\mathbf{x}_n|\tilde{\mathbf{x}}_n) = \frac{P(\tilde{\mathbf{x}}_n|\mathbf{x}_n)P(\mathbf{x}_n)}{\int \mathrm{d}\mathbf{x}' P(\tilde{\mathbf{x}}|\mathbf{x}')P(\mathbf{x}')} \tag{S22}$$

implying that to compute this term exactly, we would require the steady state probability $P(x)$, which we do not know analytically since nonlinear processes are generally not solvable. However, using the Extended Kalman filter [8], we can approximate $\mathbf{x}_n$ for each n inductively as follows: assume that $\mathbf{x}_n|\tilde{\mathbf{x}}_n \sim \mathcal{N}(\mathbf{x}_n^a, \mathbf{V}_n)$,

$$\begin{aligned}
\mathbf{x}_{n+1}^f &= \mathbf{x}_n^a + \mathbf{v}(\mathbf{x}_n^a)\Delta t \\
\mathbf{V}_{n+1}^f &= \mathbf{Q}_n \mathbf{V}_n \mathbf{Q}_n^\intercal + \mathbf{\Sigma} \\
\mathbf{K}_{n+1} &= \mathbf{V}_{n+1}^f (\mathbf{V}_{n+1}^f + \mathbf{M})^{-1} \\
\mathbf{V}_{n+1} &= \left[\mathbf{M}^{-1} + (\mathbf{V}_{n+1}^f)^{-1}\right]^{-1} \\
\mathbf{x}_{n+1}^a &= \mathbf{x}_{n+1}^f + \mathbf{K}_{n+1}(\tilde{\mathbf{x}}_{n+1} - \mathbf{x}_{n+1}^f)
\end{aligned} \tag{S23}$$

where $\Delta t = t_{n+1} - t_n$,

$$(\mathbf{Q}_n)_{ij} = \delta_{ij} + \Delta t \frac{\mathbf{v}_i}{\mathbf{x}_j}|_{\mathbf{x}=\mathbf{x}_n^a}, \quad \mathbf{M} = \begin{pmatrix} \sigma_{\theta m}^2 & 0 \\ 0 & \sigma_{pm}^2 \end{pmatrix} \tag{S24}$$

and $\sigma_{\theta m}$, σ_{pm} are measurement errors in θ, p respectively. We can easily check that in the limit of no measurement noise $\mathbf{M} = 0$, the true values are the same as the measured values: $\mathbf{x}_n^a = \tilde{x}_n, \mathbf{V} = 0$.

The extended Kalman filter provides a method to compute $P(\mathbf{x}_n|\tilde{\mathbf{x}}_n)$ by induction, as long as we know $(\mathbf{x}_0^a, \mathbf{V}_0)$. For simplicity, we just start with $\mathbf{x}_0^a = \tilde{\mathbf{x}}_0, \mathbf{V}_0 = 0$ since the effect of the boundary term on the overall log-likelihood is extremely small as we have ~ 5000 data points per trajectory. Overall, the log-likelihood computation goes as follows: for each n, we compute

$$\begin{gathered}
-\log \mathcal{P}\left[\tilde{\mathbf{x}}(t_{n+1})|\tilde{\mathbf{x}}(t_n)\right] = \frac{1}{2}\log|2\pi\tilde{\mathbf{\Sigma}}| + \frac{1}{2}\tilde{\mathbf{D}}^\intercal \tilde{\mathbf{\Sigma}}^{-1}\tilde{\mathbf{D}} \\
\text{where } \tilde{\mathbf{D}} = \tilde{\mathbf{x}}_{n+1} - \mathbf{x}_{n+1}^f, \; \tilde{\mathbf{\Sigma}} = \mathbf{V}_{n+1}^f + \mathbf{M}
\end{gathered} \tag{S25}$$

while storing $\mathbf{x}_{n+1}^a, \mathbf{V}_{n+1}$ for future computations of $\mathbf{x}^f, \mathbf{V}^f$. Adding $-\log \mathcal{P}\left[\tilde{\mathbf{x}}(t_{n+1})|\tilde{\mathbf{x}}(t_n)\right]$ for each time step and minimizing $-\log \mathcal{P}[\tilde{\mathbf{x}}_n]$, we arrive at the Maximum likelihood estimates (the measurement errors are constrained to be the expected value of 1% and 7% for θ and p respectively). Similar to before, we perform bootstrapping statistics to compute the error bars in the parameter estimates by resampling with replacements 100 times and arrive at the following values, The (θ, p) distribution and correlations are shown in Figure S15 and Figure S16.

The Maximum Likelihood estimates are all close to the preliminary estimates in Table S2. From this, we conclude that the phenomena of the free beams and clamped beams can be explained within a consistent theoretical framework.

Parameter	ϵ	$\bar{\mu}$	γ	c	β	σ_θ
Estimates from first principles	0.35 ± 0.04	0.04 ± 0.01	1 ± 0.1	$400\nu \approx 40$	N/A	0.03 ± 0.01
Inferred from free beams	N/A	0.09 ± 0.005	N/A	$(15.5 \pm 2)\gamma$	$(15 \pm 2)\gamma$	N/A
Combined estimates	0.35 ± 0.04	0.09 ± 0.005	1 ± 0.1	15.5 ± 2	15 ± 2	0.03 ± 0.01
Inference with no constraints	0.10 ± 0.02	0.19 ± 0.02	0.43 ± 0.07	5.8 ± 0.3	12.5 ± 1	0.023 ± 0.0003

TABLE S2. Parameter estimates for clamped beams. Same as Table II of the main text, reproduced here for convenience.

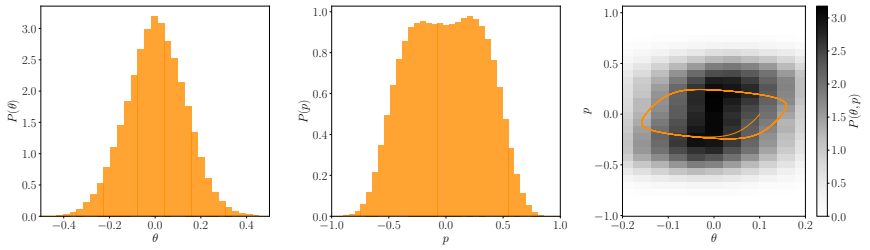

FIG. S15. (θ, p) distributions of simulations of the MLE. The deterministic trajectory with the same parameters is plotted in the right panel for comparison.

S9. PARAMETER COMPARISONS

In this section, we present the raw parameters we used to obtain the parameter values from first principles. where η comes from the property of water, l_0, ξ are measured with microscopes, E is measured with mechanical experiment (see Sec. 1 of main text) and γ, v_p come from analyzing the trajectories of single swimmers.

From there, we can estimate the intermediate parameters

$$\chi_b = \frac{4\pi\eta}{\sqrt{2\xi/l_0}}, \quad \chi_s = \frac{8\pi\eta}{3\sqrt{2\xi/l_0}}$$
$$\mu = \frac{8}{5}\pi\eta l_0(-\log(2\xi/l_0))v_p$$
$$\alpha = \nu/\xi$$

where the formula for μ comes from [9] for the motion of a sphere close to a wall. We can estimate ν roughly using stage-kicking experiments: the stage supporting the swimmers is kicked abruptly and we measure the amount of time for the swimmer directions to reorient. The reorientation time measured is within the time resolution of the image set-up, which is approximately $0.1s$. Recall from the main text that the hydrodynamic feedback follows the equation $\omega = |\nu\dot{\gamma}\sin(\phi)|$, where ω is the reorientation

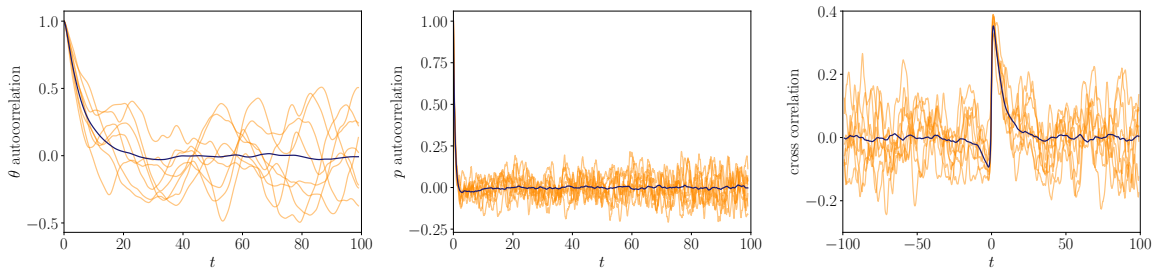

FIG. S16. Correlation functions of simulations of the MLE.

Parameter	η	l_0	ξ	E	γ	v_p
Measured value in SI units	10^{-3}	1.7×10^{-6}	10^{-7}	40	1	10^{-5}

speed $\approx 1/(0.1s)$, $\dot{\gamma}$ is the shear rate $\approx v_p/\xi \approx 10^2 s^{-1}$ and we take $\sin(\phi) \approx O(1)$. From these estimates, we arrive at a value of ν of 0.1.

The combination of the above parameters gives rise to values quoted in Table S1 and Table S2.

[1] D. J. Jeffrey and Y. Onishi. The slow motion of a cylinder next to a plane wall. *The Quarterly Journal of Mechanics and Applied Mathematics*, 34(2):129–137, 1981.

[2] S. D. Silvey. *Statistical inference*. Routledge, 2017.

[3] Olivier Andre Bauchau and James I Craig. *Structural analysis: with applications to aerospace structures*, volume 163. Springer Science & Business Media, 2009.

[4] Jinichi Nagumo, Suguru Arimoto, and Shuji Yoshizawa. An active pulse transmission line simulating nerve axon. *Proceedings of the IRE*, 50(10):2061–2070, 1962.

[5] Richard FitzHugh. Mathematical models of excitation and propagation in nerve. *Biological engineering*, 9:1–85, 1969.

[6] C. Gardiner. *Stochastic methods*, volume 4. Springer Berlin Heidelberg, 2009.

[7] Zhe Chen et al. Bayesian filtering: From kalman filters to particle filters, and beyond. *Statistics*, 182(1):1–69, 2003.

[8] Gabriel A Terejanu et al. Extended kalman filter tutorial. *University at Buffalo*, 27, 2008.

[9] Arthur Joseph Goldman, Raymond G Cox, and Howard Brenner. Slow viscous motion of a sphere parallel to a plane wall—i motion through a quiescent fluid. *Chemical engineering science*, 22(4):637–651, 1967.